

Multimodal microscopy using 'half and half' contact mode and ultrasonic force microscopy

This content has been downloaded from IOPscience. Please scroll down to see the full text.

2014 Nanotechnology 25 335708

(<http://iopscience.iop.org/0957-4484/25/33/335708>)

View [the table of contents for this issue](#), or go to the [journal homepage](#) for more

Download details:

This content was downloaded by: nwilson

IP Address: 137.205.165.224

This content was downloaded on 12/01/2015 at 18:49

Please note that [terms and conditions apply](#).

Multimodal microscopy using ‘half and half’ contact mode and ultrasonic force microscopy

M S Skilbeck¹, A J Marsden¹, G Cao², I A Kinloch², R J Young²,
R S Edwards¹ and N R Wilson¹

¹Department of Physics, University of Warwick, Coventry CV4 7AL, UK

²School of Materials, University of Manchester, Manchester M13 9PL, UK

E-mail: neil.wilson@warwick.ac.uk


Received 28 March 2014, revised 5 June 2014

Accepted for publication 9 June 2014

Published 30 July 2014

Abstract

Advances in the design and fabrication of multifunctional nanostructured materials require characterization techniques capable of simultaneously mapping multiple material properties with nanoscale resolution. We show that this can be achieved by combining nanomechanical information from ultrasonic force microscopy (UFM) with simultaneously acquired friction force and conductivity measurements from contact mode scanning. This utilizes a ‘half and half’ approach, where the AFM is operated alternatively in UFM and contact mode, with the switching rate sufficiently fast that simultaneous contact mode and UFM information is acquired at each pixel of an image. We demonstrate the potential of such a multimodal approach through its application to composite systems consisting of graphene islands on a copper surface, single-walled carbon nanotubes (SWNTs) on a silicon oxide substrate, and a graphene epoxy composite. The half and half approach enables the friction force to be measured without topographical cross-talk. Application to the SWNT sample reveals a further advantage; due to the superlubricity of UFM it enables standard contact mode imaging techniques to be applied to delicate samples.

 Online supplementary data available from stacks.iop.org/NANO/25/335708/mmedia

Keywords: atomic force microscopy, ultrasonic force microscopy, graphene, carbon nanotubes


(Some figures may appear in colour only in the online journal)

1. Introduction

Technological needs are driving the development of multifunctional nanostructured materials, where multiple material properties are enhanced through control of material at the nanometre scale. For example, fillers such as graphene or nanotubes can be added to composites to enhance mechanical properties and at the same time increase thermal and electrical conductivity [1, 2]. Similarly, in phase-change materials,

changes in functional properties such as conductivity are induced by changes in structural, and hence mechanical, properties [3]. Thus there is a need for characterization techniques that are capable of simultaneously correlating multiple material properties at nanoscale resolution.

Scanning probe microscopy is ideally suited to such a challenge. It is routinely used to investigate nanoscale sample topography, but increasingly is also being applied as a tool for measuring functional properties and correlating them to sample structure. Well-established examples include mechanical mapping through analysis of indentation forces [4], conductivity mapping through conductive AFM (cAFM) [5], friction force microscopy, magnetic force microscopy, piezo-electric force microscopy etc [6]. At a general level,

 Content from this work may be used under the terms of the [Creative Commons Attribution 3.0 licence](http://creativecommons.org/licenses/by/3.0/). Any further distribution of this work must maintain attribution to the author(s) and the title of the work, journal citation and DOI.

these imaging modes can be classified as static or dynamic (e.g. contact mode imaging is static, whilst tapping mode is dynamic) and as contact or intermittent/non-contact. Typically they can only be applied simultaneously if they fall into the same classification, e.g. contact mode topography can be measured at the same time as friction and conductivity (all static, contact) but not alongside mechanical mapping (dynamic).

Here we demonstrate a new approach to multifunctional imaging that combines mechanical information from ultrasonic force microscopy (UFM, dynamic, intermittent contact) with contact mode (static, contact) signals. We demonstrate this through combined UFM and friction force microscopy of graphene on copper, UFM and conductivity mapping of a single-walled carbon nanotube network (SWNTs), and UFM, friction force microscopy and conductivity mapping of a graphene nanoplatelet epoxy composite. Imaging of the nanotube network demonstrates a further advantage of this approach, as it enables contact mode techniques to be applied to delicate samples that cannot be easily imaged in conventional contact mode.

2. Experimental Methods

2.1. UFM

All AFM images were acquired with an Asylum Research MFP-3D AFM. For ultrasonic excitation the samples were bonded with salol (phenyl salicylate) to a disk piezoelectric transducer (made by PI Ceramic using material PIC255) operating in thickness expansion mode with a nominal resonance frequency of 8 MHz. The transducer was driven using a Tektronix AFG3022B arbitrary function generator with the UFM driving frequency tuned to give the biggest cantilever response, which corresponds to the transducer resonance. The amplitude modulation took a half sine shape, as illustrated in figure 2, with a frequency of 4 kHz and maximum amplitude for the signal generator, i.e. $20 V_{pp}$, giving typical surface amplitudes of approximately 1 to 10 nm. For images where more than one lock-in amplifier was needed, a Stanford Research Systems SR830 was used in addition to the AFM's internal lock-in amplifier.

For the graphene on copper measurements the tips used were Mikromasch NSC18 tips (nominal normal spring constant 3 Nm^{-1} , resonance frequency 75 kHz and tip radius 8 nm), which were calibrated using the Sader method [7] for the normal spring constant and the wedge calibration method [8] on a Mikromasch TGF11 trapezoidal calibration grid for the lateral spring constant. The lateral amplitude (amplitude of change in lateral signal due to modulation of ultrasound, as discussed in section 3.2) was acquired with the internal lock-in amplifier and the UFM signal was acquired with the external lock-in amplifier, both running at the modulation frequency.

For the conductive measurements an Asylum Research ORCA tip holder was used for current amplification; for the SWNT results a dual gain ORCA with gains of 10^6 VA^{-1} and

10^9 VA^{-1} was used whilst for the graphene nanoplatelet epoxy composite results a standard ORCA with a gain of $5 \times 10^6 \text{ VA}^{-1}$ was used. The tips used were platinum coated NSC18 (specifications as above) for the nanotube sample and platinum coated Mikromasch CSC37 tips (longest cantilever, nominal normal spring constant 0.3 Nm^{-1} , resonance frequency 20 kHz and tip radius 8 nm) for the graphene nanoplatelet epoxy composite sample. The bias voltage was applied to a gold contact on the nanotube sample and directly to the top surface of the composite sample.

2.2. Samples

Low pressure chemical vapour deposition (LP-CVD) [9] on copper foils (99.5% purity, 0.025 mm thick, Alfa Aesar product number 46365) was used to grow the graphene on copper samples, as described in [10]. The process started with an electropolish in a solution of orthophosphoric acid and urea [11] (10 s at 5 V, $\sim 1.5 \text{ A}$). The foils were then placed in a quartz tube under vacuum (10^{-1} mbar), with 20 sccm hydrogen flowing throughout the growth process. The quartz tube was heated in a tube furnace and after reaching 1000°C the samples were annealed for 20 min, followed by introducing 2 sccm methane. After this, the methane flow was stopped and the sample was cooled to room temperature.

SWNTs were grown on a silicon oxide on silicon substrate by catalysed chemical vapour deposition (cCVD) using an iron catalyst and methane as feedstock, as described in [12].

The graphene nanoplatelet epoxy composite was made using xGnP graphene nanoplatelets from XG Sciences, grade M25 (average particle diameter and thickness of $25 \mu\text{m}$ and 6 nm, respectively, according to manufacturer information) in Araldite LY 556 epoxy with hardener XB 3473, with 8% graphene by weight. The graphene nanoplatelets were stirred into the epoxy using an IKA EUROSTAR shear mixer for 1 hour at 2000 rpm. The hardener was then added (at a weight ratio of 23:100 to the epoxy) and stirred for a further 10 min at 2000 rpm. The mixture was then sonicated at 37 kHz for 10 min, followed by vacuum degassing in an oven at 60°C for 10 min. The mixture was poured into a mold and cured at 140°C for 12 hours. Once cooled to room temperature the sample was removed from the mould and cut to size. The images presented here are of a cut face.

3. Results and Discussion

3.1. Conventional UFM imaging

UFM was developed as a tool for high resolution mechanical mapping, giving stiffness information about the surface of a sample with the additional benefit of visualization of sub-surface features [13–17]. A schematic of the UFM set up is shown in figure 1. A piezoelectric transducer under the sample drives it to oscillate; in standard UFM the ultrasonic excitation is modulated such that half of the time it is on and half of the time it is off (and so imaging is dynamic,

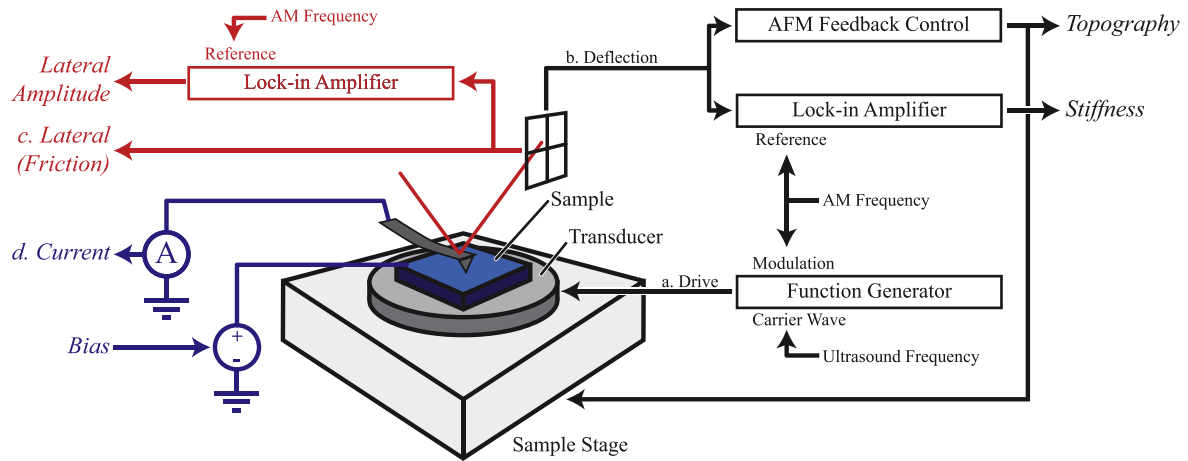


Figure 1. Schematic of the UFM setup. The right hand side of the image shows the standard UFM setup and the left hand side corresponds to the addition of simultaneous friction and conductivity measurement techniques. Outputs labelled with letters correspond to the signals in figure 2.

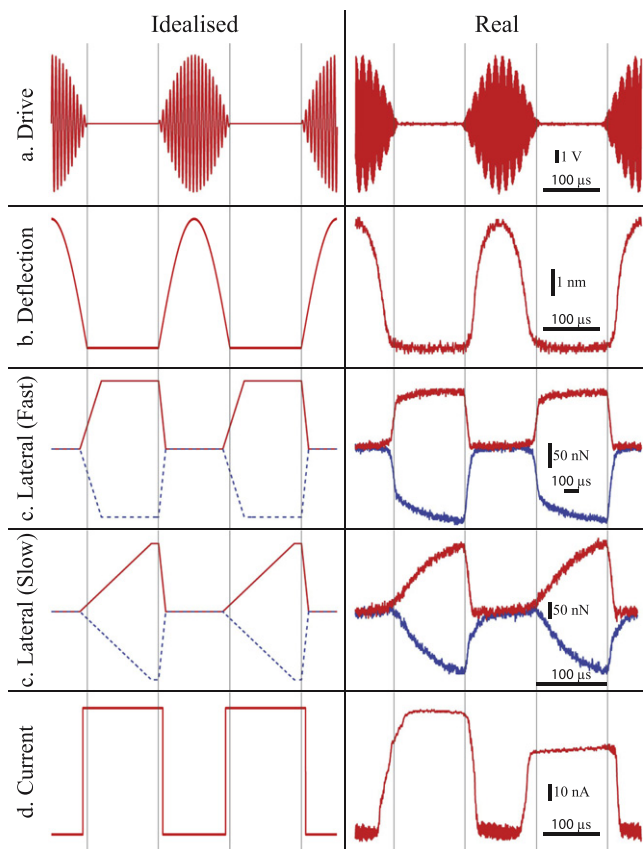


Figure 2. Idealized and captured oscilloscope traces of the signals generated during UFM operation. The idealized traces are simplified to show the basic structure of each signal. All the traces are lined up such that their modulation phase matches. On the lateral traces, the two lines (red and blue) correspond to the trace and retrace scan directions, and ‘slow’ and ‘fast’ refer to the tip velocities of $25 \mu\text{ms}^{-1}$ and $125 \mu\text{ms}^{-1}$ respectively, though the modulation frequencies are also different, resulting in the fast trace having a tip motion 25 times faster relative to the modulation phase. Lettering corresponds to the outputs labelled in figure 1.

intermittent contact), in order to decouple the UFM response from topography induced changes in deflection, as described below.

Figure 2 shows the idealized and real signals that result during UFM operation. A typical ultrasonic drive signal is given in figure 2(a). Standard ultrasonic excitation is at a frequency in the range 2–10 MHz, modulated at frequencies of 2–5 kHz such that at each pixel in an image there are several cycles of ultrasound on/ultrasound off. The ultrasonic excitation is at frequencies well above the cantilever resonance, hence the cantilever is unable to respond and effectively becomes stationary during an oscillation period, resulting in the tip being alternately indented into and retracted from the sample. The effective force being applied to the cantilever by the sample is then the time-averaged force of the tip–sample interaction during the oscillation. Due to the shape of the nonlinear tip–sample interaction force curve, this average force is always greater than in the static case, resulting in an additional deflection of the cantilever. This can be seen in figure 2(b), where the deflection increases as the ultrasound amplitude increases. As shown in figure 1, the change in deflection due to the ultrasonic excitation is measured by a lock-in amplifier, giving the UFM signal. This is dependent on the magnitude of the sample oscillation and on the shape of the force curve, which in turn is dependent on the sample stiffness. Stiffer samples have a steeper force curve, resulting in a higher average force and therefore an increase in the ultrasonically induced deflection; hence the UFM signal gives stiffness contrast.

By modulating the ultrasonic excitation such that it is periodically on then off, the amplitude of the change in deflection at the modulation frequency can be measured as the UFM signal, whilst the time averaged, i.e. low pass filtered, deflection signal can be used as the topographical feedback signal, as in conventional contact mode. However, the modulation of the ultrasonic excitation signal also leads to a ‘half and half’ operation of the AFM, where half of the time it is in contact mode and the other half it is in ultrasonic force mode.

As the period at which it is alternately in UFM or contact AFM mode is less than the time between pixels, this means that signals usually acquired during contact mode scanning can be acquired simultaneously with UFM stiffness information.

3.2. Combined friction and UFM measurements

In traditional friction force microscopy the fast scan axis is chosen such that it is perpendicular to the cantilever axis, meaning that friction causes torsional bending of the cantilever. This torsional bending is picked up as the lateral deflection signal on a conventional four quadrant photodiode detector. The torsional moment acting on the cantilever is dependent on the load force, the coefficient of friction between the tip and surface, and also on the slope of the sample. As a result, to decouple the friction signal from the topography, friction should be measured from the difference between the trace and retrace lateral signals, which removes the effect of slope to first order [8].

Figure 2(c) shows the lateral forces measured when scanning in modulated UFM mode. Comparing the lateral force, figure 2(c), with the ultrasonic excitation, it can be seen that the friction force disappears (the trace and retrace signals overlap) when the ultrasonic excitation exceeds a critical value. This is the origin of the superlubricity in UFM, previously reported by Dinelli *et al* [18], whereby once the sample excitation amplitude is sufficient such that the tip periodically detaches from the surface, no lateral force can be maintained between the tip and the sample [19]. During the detachment the torsion in the cantilever restores to the central position, which is typically a faster process than the increase in torsion due to the motion of the sample during contact, resulting in zero lateral deflection due to ultrasound and no lateral force applied to the sample [20]. Using this it has been shown that UFM can be used to image delicate samples, such as polystyrene, that are damaged by conventional contact mode scanning [17].

However, when the ultrasonic amplitude is reduced below this threshold the tip is in continuous contact with the sample, and friction can start to torsionally bend the cantilever and hence induce a lateral deflection. The time taken for this lateral deflection to reach its steady state value depends on the scan rate and the torsional stiffness of the cantilever. Hence, initially, an almost linearly increasing lateral force is observed, the slope of which depends on the scan rate, as can be seen through comparison between the fast and slow scan rate traces shown in figure 2(c). Once the torsion reaches the friction limit the lateral signal becomes constant, the value of which varies depending on the load force and coefficient of friction, as expected (see figure S1 of the supplementary information for quantitative evaluation). When the ultrasound turns on again, the cantilever torsion rapidly decreases until the superlubricity threshold is reached, at which point the lateral force becomes zero again. The tip thus moves across the surface in a stick-slip motion. These results appear similar to results seen in acoustic friction force microscopy [21] and ultrasonic friction force microscopy [22], however, these both

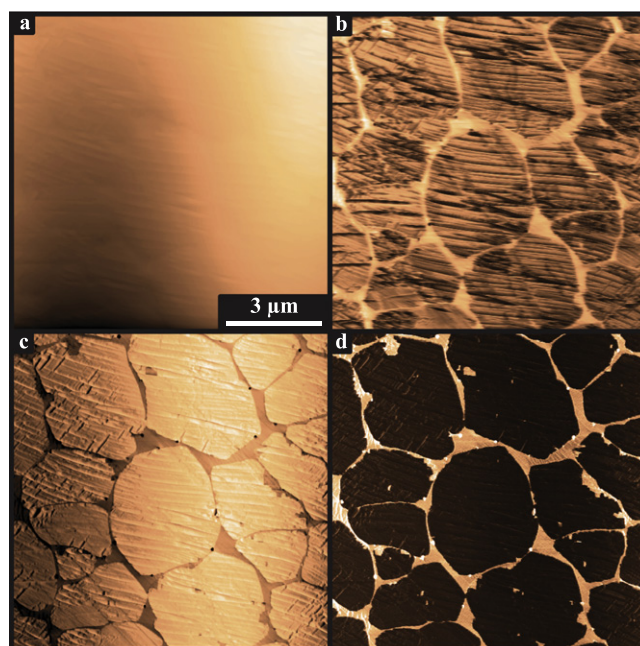


Figure 3. Simultaneously captured images of copper foil with graphene islands. The channels shown and their corresponding full data scales are (a) height, 600 nm, (b) UFM response, 10 nm, (c) lateral (cantilever torsion), 400 nN, and (d) lateral amplitude, 50 nN. All are taken in the retrace direction.

rely on the use of shear ultrasound wavemodes, as opposed to the longitudinal ultrasound wavemodes used here. Significant coupling between the longitudinal and shear modes is unlikely, i.e. the longitudinal mode will be the dominant mode, and the results are consistent with previously published work regarding ultrasonic out of plane surface oscillations [19].

As the friction still affects the lateral signal for part of the time, friction can be recorded during UFM operation. This is achieved in the same way as traditional friction force microscopy, where the average lateral trace and retrace values are taken at each point. However, the modulation of the lateral force signal due to the ultrasound being turned on and off naturally leads to an alternative approach; using a lock-in amplifier to measure the oscillation in the lateral force signal, which is proportional to the friction force. This lateral amplitude value has a significant advantage in that, unlike conventional friction force microscopy, it is independent of the topography as the topographical influence on the lateral signal is a DC offset.

Figure 3 shows an example of simultaneously measured topography, UFM and friction force maps. The sample is graphene grown on copper foil by chemical vapour deposition (CVD) [9]; the growth was halted before a complete monolayer of graphene was formed, such that the surface is partially covered in single atom thick graphene islands a few micrometres in diameter. The graphene islands are not directly visible in the topography image, figure 3(a), which is dominated by the fact that the copper surface is rough with large undulations from the cold rolling process used to make the foil [10, 11]. In the UFM response, figure 3(b), contrast due to the graphene islands can be seen. Interestingly, the

graphene is darker in contrast than the surrounding bare copper surface, indicating a lower UFM response and hence softer surface. Force curves showed that the adhesion was unchanged across the sample, and previous work has shown that if graphene is fully delaminated from a surface the ultrasound signal completely disappears [23]. This suggests that the lower UFM response on graphene is due to a comparatively soft interface between the graphene and copper, consistent with the graphene being decoupled from the copper (but not delaminated) and only weakly physisorbed to it [10]. The lateral force, figure 3(c), also clearly resolves the graphene islands due to their low friction [24] (note that due to the scan direction, the colour scale is inverted and lighter contrast corresponds to higher friction). All of the images in figure 3 were taken simultaneously in a single pass and in one scan direction; as expected, the lateral force image, figure 3(c), thus shows large cross-talk with the topography. The lateral amplitude, figure 3(d), shows similar clear frictional contrast (here darker contrast is lower friction), but with no topographical cross-talk. This demonstrates that the lateral amplitude signal can be used directly as a measure of the local friction on the surface, without the need to subtract the trace from the retrace signals. Quantitative analysis of the UFM lateral force and lateral amplitude is given in the supplementary information, demonstrating that they can both be used to quantify the friction force.

The ability to directly measure multiple material properties simultaneously in one pass is extremely useful, as this allows exact spatial correlation and minimizes the effect of changing tip geometry. It is particularly advantageous for AFM scanners not operated under closed loop conditions, or for samples with large drift, where it is not possible to accurately compare points from the two scan directions; this is often apparent when subtracting trace and retrace lateral force images to form a friction image, where a small misalignment in points between the scan directions results in blurring and a loss of resolution.

3.3. Combined conductive and UFM measurements

cAFM is performed by applying a potential difference between a conducting tip (typically covered with a thin metal coating) and the sample surface and measuring the resultant current flow between them. cAFM is usually applied during contact mode as it relies on the tip being in contact with the sample.

Figure 2(d) shows the measured current between tip and surface as the ultrasonic excitation is modulated. The current flows during the period in which ultrasound is off and hence the tip is in contact with the surface. No current is measured when the ultrasound is on, with the onset of zero current correlating to the onset of superlubricity, when the tip is periodically retracted from the surface. It is unclear why the observed current falls to zero, as the tip does periodically contact the sample whilst the ultrasound is applied; we speculate that this is due to the virtual earth amplifier used to measure the current. However, the measured presence of current during the contact period indicates that conductivity

mapping can be performed simultaneously to UFM, with the additional advantage of superlubricity to reduce tip and sample damage. This is of particular importance for cAFM, as the integrity of the metal coating is critical for current flow between tip and sample.

Figure 4 shows combined UFM and cAFM of a SWNT network on an insulating silicon oxide substrate. The SWNTs were grown directly onto the substrate by cCVD [12]. Such networks are of interest for applications such as flexible electronics [25], for example transparent conductors and sensors [26]. The cCVD growth process results in random growth of metallic and semiconducting SWNTs; for sensor applications the current flow should be dominated by the semiconducting SWNT (whose conductance is highly dependent on the environment), whilst for transparent conductors the more highly conductive metallic SWNTs should dominate. For both applications, understanding conduction through the contacts between nanotubes is imperative, as these usually dictate the electrical response. The high spatial resolution of cAFM is thus, in principle, ideal for studying such networks. Although there have been some prior reports, e.g. [27], cAFM analysis of the networks is usually complicated by the fact that the nanotubes are easily damaged by contact mode AFM scanning and hence alternatives to conventional contact mode cAFM have to be used [28]. However, due to the superlubricity induced by UFM, it is straightforward to map the conductivity of the SWNT network with minimal damage by combined UFM and cAFM, and this is performed here. Measurements were repeated many times without any major damage to the SWNTs, unlike when scanning in conventional contact mode, as demonstrated by figures S2 and S3 in the supplementary information.

The topography image, figure 4(a), shows the intersecting network of SWNTs, each typically 1–2 nm in height. The raised region in the top right of the image is a residue of the lithographic process used to deposit the gold, which also reduces the conductivity. In the UFM response, figure 4(b), the SWNTs appear to be softer (darker contrast) than the silicon oxide substrate; this could be due to the modified contact shape of the tip on the nanotube or due to the lower radial stiffness of the nanotubes. However, the conductivity map, figure 4(c), clearly reveals the conductive pathways through the SWNT network. Note that the colour scale is logarithmic with respect to current, such that the measured currents vary over more than five orders of magnitude. The conductivity measurements were remarkably consistent, both across a single image and after multiple scans (an example is given in figure S3 of the supplementary information), which is surprising considering that metal coatings of tips, such as the Pt coating used here, are prone to wear [29]. This indicates that UFM not only reduces damage to the sample but also reduces damage to the tip.

From figure 4(c) it is possible to identify the metallic and semiconducting nanotubes and the differences in contact resistances between them. A metallic SWNT is marked by the blue arrow; the current flow along this SWNT is roughly constant, indicating that it is limited by resistances in the

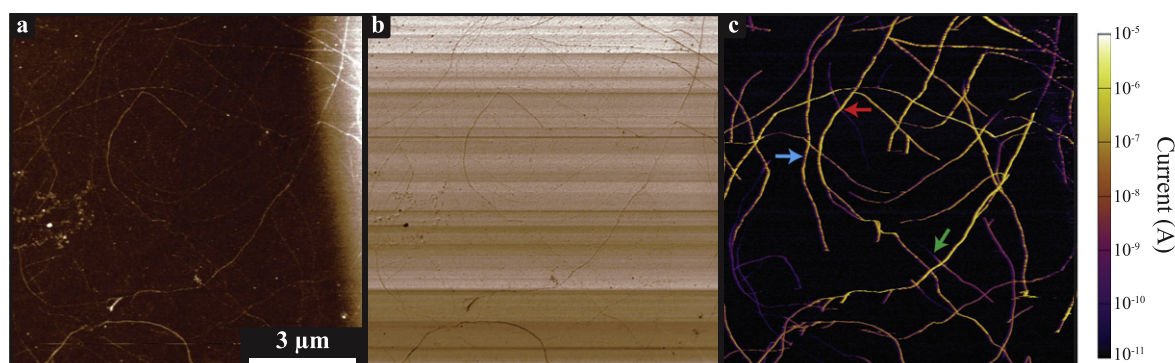


Figure 4. Simultaneously captured images of carbon nanotubes on a silicon substrate. The nanotube network is connected to a gold pad to the right of the image, which is held at a 2 V bias. The channels shown and their corresponding full data scales are (a) height, 6 nm, (b) UFM response, 1.5 nm, and (c) logarithmic current, scale given on the image. The red arrow on (c) marks a clear example of high contact resistance between nanotubes, the blue arrow shows a metallic nanotube with low contact resistance and the green arrow shows a semiconducting nanotube.

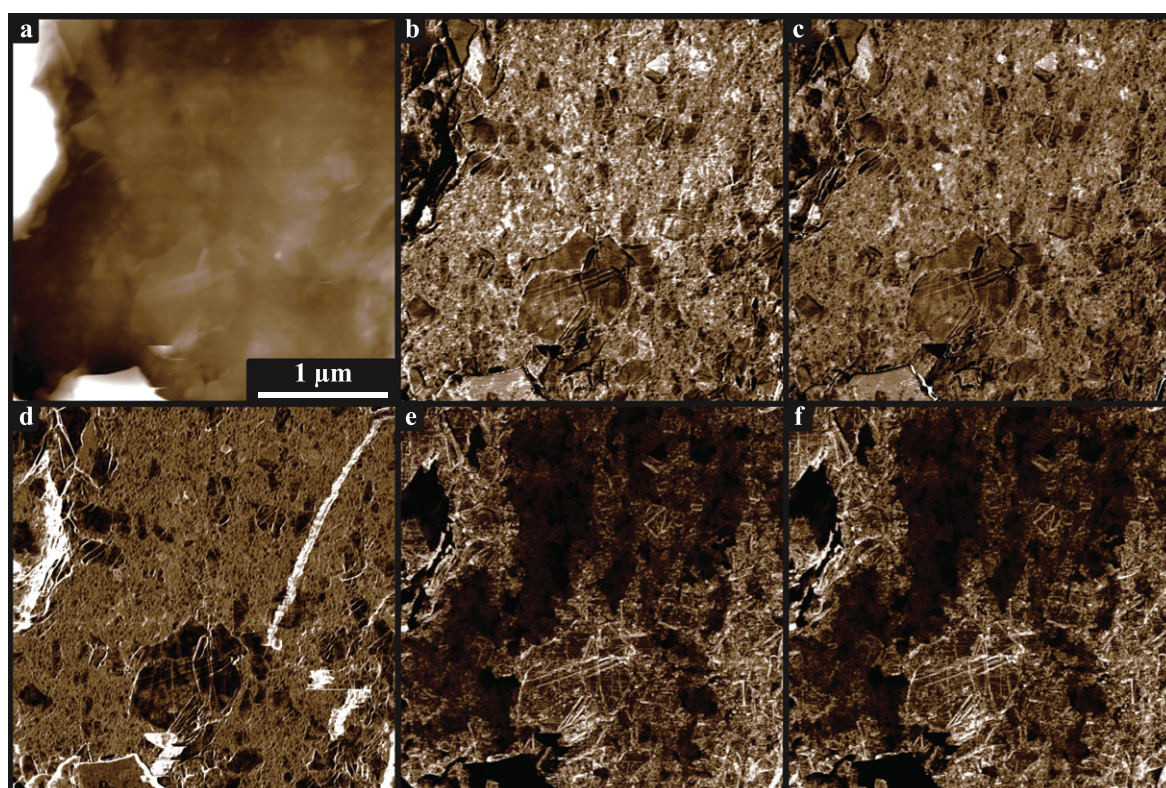


Figure 5. Simultaneously captured images of a graphene nanoplatelet epoxy composite. The top of the sample is connected to a wire which is held at a 0.5 V bias. The channels shown and their corresponding full data scales are (a) height trace, 150 nm, (b), (c) UFM response trace and retrace respectively, 0.5 nm with a minimum value of 0.5 nm, (d) lateral trace minus retrace, 4 mV, and (e), (f) current trace and retrace respectively, 2 μ A.

network closer to the electrode, and similar to the neighbouring SWNTs, suggesting a low resistance at the junction indicated. By comparison, the red arrow points to a high resistance junction where the current drops by 3 orders of magnitude within 50 nm of the junction and then stays roughly constant. The current along the SWNT labelled by the green arrow decays exponentially with distance away from the junction, indicating a semiconducting SWNT (see figure S4 in the supplementary information for line profiles of the current flow along these SWNTs). Due to the multiple

connections to each nanotube in this network, it is not easy here to quantitatively extract contact resistances and the resistivity of individual SWNTs. However, this would be possible on lower density networks.

3.4. Combining multiple techniques

The half and half approach enables multiple contact mode techniques to be acquired simultaneously with UFM. Figure 5 shows combined UFM, friction, and cAFM measurements on

a graphene nanoplatelet epoxy composite. The composite is made from multi-layer graphene nanoplatelets with flakes of nominal average diameter 25 μm and thickness 6 nm, randomly dispersed at comparatively high loading fraction (8 % by weight) in an epoxy matrix (see section 2.2 for more details). The sample was cut for UFM analysis to study the dispersion and connectivity of the graphene nanoplatelets within the matrix. The height image, figure 5(a), shows features that look like they could be due to graphene nanoplatelets but as the sample is comparatively rough it is difficult to identify them with any confidence. The UFM response, figures 5(b) and (c), shows much more detail with clear variations in the sample stiffness. Both the trace and retrace images are shown, figures 5(b) and (c) respectively, demonstrating the exact reproducibility of the result. The friction image, formed from subtracting the lateral deflection signal in the trace and retrace directions and shown in figure 5(d), gives interesting complementary information to the UFM image. There is a strong correlation between the regions of lower friction and the regions of lower UFM amplitude and we thus identify them as regions where graphene is present at the surface, an assignment reinforced by the topography image. Note that this is highlighting graphene nanoplatelets directly at the surface and it is likely that they also extend below the surface, however, it does seem to indicate that there has been some fragmentation of the xGnP graphene nanoplatelets during shear mixing.

It is interesting that the graphene nanoplatelets show a lower UFM response, implying that they are softer than the surrounding epoxy matrix. This was consistent across many measurements with several different tips (see figure S5 in the supplementary information for a further example). The *c*-axis, i.e. out of plane, Young's modulus of graphite is lower than copper but higher than epoxy, so in this instance we would naively expect the graphene to show greater UFM amplitude, i.e. lighter contrast. As with the graphene on copper sample, delamination of the graphene nanoplatelets is not seen as the UFM signal does not fall to zero. The lower UFM response could be due to poor acoustic coupling between the nanoplatelets at the surface and the epoxy which would reduce the surface ultrasonic amplitude. Alternatively it could be due to a weak interface between the graphene and epoxy, softer than the interplanar interface of graphite and also softer than bulk epoxy, resulting in reduced out of plane stiffness.

Further information can be seen in the current images, figures 5(e) and (f). Again both the trace and retrace image are shown, demonstrating the reproducibility of the result. The sample could be scanned for several hours under these conditions without degradation of the sample or tip and maintaining reproducibility of the current image. The correlation between features in the current image and the other image channels is again strong, but it also reveals new information. As expected, there is higher current around the exposed graphene nanoplatelets seen in figures 5(e) and (f). Additionally, further structure can be seen in these current images, with larger regions of different current levels, which is likely due to the local network structure of the graphene nanoplatelets resulting in some surface sheets having poorer

conductive pathways to the bulk. The edges of many of the platelets appear to have enhanced current flow, though this is correlated to changes in topography, making it likely that these features are due to a tip effect. The loading fraction of graphene here is high, substantially greater than the percolation threshold, which is consistent with the high level of conductivity seen across the image. Combined, these multiple channels give rich information on the dispersion and percolation of the graphene nanoplatelet epoxy composite.

4. Conclusions

We have shown that UFM can be combined with contact mode AFM techniques for multifunctional imaging, including for the application of contact mode imaging techniques on delicate samples. UFM has previously been applied to map the stiffness of a variety of systems, such as investigating stress induced mechanical property variations in hard samples like semiconductor nanodots [30, 31] or damascene structures [32], as well as softer samples such as carbon fibres in an epoxy matrix [33] and rubber inclusions in PMMA [34]. It has also been shown to be sensitive to subsurface defects, including surface film delaminations [17] and lattice defects [16]. We have combined UFM with friction force microscopy and cAFM to simultaneously map multiple material properties on graphene on copper, delicate SWNT samples, and graphene nanoplatelet epoxy composites, with nanoscale resolution. This work demonstrates the extension of UFM to multimodal imaging, enabling high spatial resolution mapping of multifunctional materials. More generally, with the new generation of digital AFM controllers, the 'half and half' concept could be extended to combine multiple different imaging modes.

Acknowledgments

We acknowledge support from the University of Warwick through a Chancellor scholarship to MSS, support from the EPSRC through grant EP/J015202/1, and Oxford Instruments Asylum Research, Inc. for loan of the dual gain ORCA.

References

- [1] Qian H, Greenhalgh E S, Shaffer M S and Bismarck A 2010 Carbon nanotube-based hierarchical composites: a review *J. Mater. Chem.* **20** 4751–62
- [2] Young R J, Kinloch I A, Gong L and Novoselov K S 2012 The mechanics of graphene nanocomposites: a review *Compos. Sci. Technol.* **72** 1459–76
- [3] Raoux S, Welnic W and Ielmini D 2010 Phase change materials and their application to nonvolatile memories. *Chem. Rev.* **110** 110–67
- [4] Butt H J, Cappella B and Kappl M 2005 Force measurements with the atomic force microscope: technique, interpretation and applications *Surf. Sci. Rep.* **59** 1–152

- [5] Shafai C, Thomson D J, Simard-Normandin M, Mattiussi G and Scanlon P J 1994 Delineation of semiconductor doping by scanning resistance microscopy *Appl. Phys. Lett.* **64** 342–4
- [6] Meyer E, Hug H and Bennewitz R 2004 *Scanning Probe Microscopy: The Lab on a Tip* (Berlin: Springer)
- [7] Sader J E, Chon J W and Mulvaney P 1999 Calibration of rectangular atomic force microscope cantilevers *Rev. Sci. Instrum.* **70** 3967–9
- [8] Varenberg M, Etsion I and Halperin G 2003 An improved wedge calibration method for lateral force in atomic force microscopy *Rev. Sci. Instrum.* **74** 3362–7
- [9] Li X *et al* 2009 Large-area synthesis of high-quality and uniform graphene films on copper foils *Science* **324** 1312–4
- [10] Wilson N R *et al* 2013 Weak mismatch epitaxy and structural feedback in graphene growth on copper foil *Nano Res.* **6** 99–112
- [11] Zhang B, Lee W H, Piner R, Kholmanov I, Wu Y, Li H, Ji H and Ruoff R S 2012 Low-temperature chemical vapor deposition growth of graphene from toluene on electropolished copper foils *ACS Nano* **6** 2471–6
- [12] Edgeworth J P, Wilson N R and Macpherson J V 2007 Controlled growth and characterization of two-dimensional single-walled carbon-nanotube networks for electrical applications *Small* **3** 860–70
- [13] Yamanaka K, Ogiso H and Kolosov O V 1994 Ultrasonic force microscopy for nanometer resolution subsurface imaging *Appl. Phys. Lett.* **64** 178–80
- [14] Kolosov O and Yamanaka K 1993 Nonlinear detection of ultrasonic vibrations in an atomic force microscope *Japan J. Appl. Phys.* **32** L1095–8
- [15] Rabe U and Arnold W 1994 Acoustic microscopy by atomic force microscopy *Appl. Phys. Lett.* **64** 1493–5
- [16] Yamanaka K 1996 UFM observation of lattice defects in highly oriented pyrolytic graphite *Thin Solid Films* **273** 116–21
- [17] Dinelli F, Castell M R and Ritchie D A 2000 Mapping surface elastic properties of stiff and compliant materials on the nanoscale using ultrasonic force microscopy *Phil. Mag. A* **80** 2299–323
- [18] Dinelli F, Biswas S K, Briggs G A D and Kolosov O V 1997 Ultrasound induced lubricity in microscopic contact *Appl. Phys. Lett.* **71** 1177–9
- [19] Hesjedal T and Behme G 2002 The origin of ultrasound-induced friction reduction in microscopic mechanical contacts *IEEE Trans. Ultrason. Ferroelectr. Frequency Control* **49** 356–64
- [20] Robinson B J, Kay N D and Kolosov O V 2013 Nanoscale interfacial interactions of graphene with polar and nonpolar liquids *Langmuir* **29** 7735–42
- [21] Scherer V, Bhushan B, Rabe U and Arnold W 1997 Local elasticity and lubrication measurements using atomic force and friction force microscopy at ultrasonic frequencies *IEEE Trans. Magn.* **33** 4077–9
- [22] Cuberes M T and Martinez J J 2007 Mechanical-diode mode ultrasonic friction force microscopy *J. Phys. Conf. Ser.* **61** 224–8
- [23] Robinson B J, Rabot C, Mazzocco R, Delamoreanu A, Zenasni A and Kolosov O V 2014 Nanomechanical mapping of graphene layers and interfaces in suspended graphene nanostructures grown via carbon diffusion *Thin Solid Films* **550** 472–9
- [24] Marsden A J, Phillips M and Wilson N R 2013 Friction force microscopy: a simple technique for identifying graphene on rough substrates and mapping the orientation of graphene grains on copper *Nanotechnology* **24** 255704
- [25] Park S, Vosguerichian M and Bao Z 2013 A review of fabrication and applications of carbon nanotube film-based flexible electronics *Nanoscale* **5** 1727–52
- [26] Snow E S, Perkins F K and Robinson J A 2006 Chemical vapor detection using single-walled carbon nanotubes *Chem. Soc. Rev.* **35** 790–8
- [27] Nirmalraj P N, Lyons P E, De S, Coleman J N and Boland J J 2009 Electrical connectivity in single-walled carbon nanotube networks *Nano Lett.* **9** 3890–5
- [28] Stadermann M *et al* 2004 Nanoscale study of conduction through carbon nanotube networks *Phys. Rev. B* **69** 201402
- [29] Palacio M and Bhushan B 2008 Nanomechanical and nanotribological characterization of noble metal-coated AFM tips for probe-based ferroelectric data recording *Nanotechnology* **19** 105705
- [30] Cuberes M T, Stegemann B, Kaiser B and Rademann K 2007 Ultrasonic force microscopy on strained antimony nanoparticles *Ultramicroscopy* **107** 1053–60
- [31] Kolosov O V, Castell M R, Marsh C D, Briggs G A D, Kamins T I and Williams R S 1998 Imaging the elastic nanostructure of Ge islands by ultrasonic force microscopy *Phys. Rev. Lett.* **81** 1046–9
- [32] Geer R E, Kolosov O V, Briggs G A D and Shekhawat G S 2002 Nanometer-scale mechanical imaging of aluminum damascene interconnect structures in a low-dielectric-constant polymer *J. Appl. Phys.* **91** 4549–55
- [33] Dinelli F and Assender H E 1999 Elastic mapping of heterogeneous nanostructures with ultrasonic force microscopy (UFM) *Surf. Interface Anal.* **27** 562–7
- [34] Porfyraakis K, Kolosov O V and Assender H E 2001 AFM and UFM surface characterization of rubber-toughened poly (methyl methacrylate) samples *J. Appl. Polym. Sci.* **82** 2790–8